Dynamic Surface Restructuring in Cu(Au) Alloys Driven by Oxygen-Mediated Au mobility

Dongxiang Wu[1], Xianhu Sun[1], Lianfeng Zou[1], Dmitri Zakharov[2], Judith C. Yang[2,3], Guangwen Zhou[1]*

[1]Department of Mechanical Engineering & Materials Science and Engineering Program, State University of New York, Binghamton, New York 13902, USA

[3]Center for Functional Nanomaterials, Brookhaven National Laboratory, Upton, NY 11973, USA

[2]Department of Chemical and Petroleum Engineering, University of Pittsburgh, Pittsburgh, PA 15261, USA

Abstract

Alloying plays a crucial role in tuning the surface properties of metals, but the atomic-level mechanisms by which alloying elements influence surface structure dynamics under reactive conditions remains elusive. Using Cu(Au) in oxidizing environments as a model system, we reveal a dynamic oxygen-induced transformation of the topmost atomic layer into a periodically hill-and-valley morphology, with reversible switching between undulated and flattened surface states. These interconversions are driven by the retreat of surface Au to the subsurface during oxygen adsorption and its resegregation to the surface upon oxygen desorption. This cyclical mobility establishes a feedback loop, allowing the surface to dynamically reconfigure in response to changes in oxygen pressure. The findings offer a broadly applicable framework for understanding atomic-scale surface restructuring in alloy systems, where differences in the chemical reactivity of alloying elements drive dynamic redistribution between surface and subsurface regions. This dynamic coupling has practical implications for designing corrosion-resistant coatings and metastable nanostructures with tunable catalytic properties.

*Correspondence to: gzhou@binghamton.edu

TOC Graphic

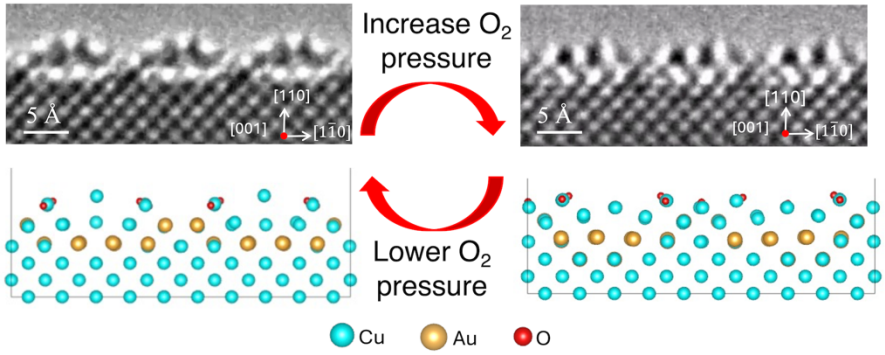

Alloying serves as a cornerstone strategy for engineering material properties, primarily through targeted element segregation to critical microstructural regions, such as exposed surfaces affecting corrosion resistance and catalytic activity, grain boundaries impacting fracture strength, and dislocations modulating plastic deformation[1-4]. Beyond these well-documented effects, here we report an alloying phenomenon—oxygen-driven atomic reconfigurations that dynamically reshape both composition and structure across the surface and subsurface of alloys. Such behavior has remained hidden due to the difficulty of capturing rapid, atomic-scale dynamics across multiple atomic planes of the surface and subsurface regions under reactive gas environments.

In situ transmission electron microscopy (TEM) has emerged as a transformative tool for probing surface segregation dynamics at the atomic scale[5-11]. Here, leveraging environmental TEM, we capture—in real time—the oxygen-triggered transformation of a flat Cu(Au) surface into a periodically undulating hill-and-valley morphology, followed by its reversible flattening in response to oxygen adsorption and desorption. By integrating atomic-resolution imaging with density functional theory (DFT), we establish that this structural metamorphosis is mechanistically governed by oxygen-mediated Au redistribution: oxygen adsorption destabilizes surface Au, driving its retreat into the subsurface, while desorption reverses this process, resegregating Au to

the surface. These operando observations expose a previously hidden feedback loop, where gas-surface reactions directly modulate noble metal mobility, which in turn regulates the surface restructuring dynamics.

The Cu-Au system serves as an ideal model due to its unique physicochemical duality. The stark contrast in oxygen affinity between Cu (highly reactive) and Au (noble) drives oxygen-mediated surface segregation: Cu preferentially oxidizes, while Au retreats into the subsurface, creating a dynamic interplay between surface and subsurface. This behavior underpins the enhanced performance of Cu-Au alloys over their monometallic counterparts in various catalytic reactions such as CO oxidation, CO_2 reduction, methanol synthesis, and the water-gas shift reaction[12-17], where dissociative oxygen adsorption—a step highly sensitive to surface structure and elemental distribution—dictates reaction efficiency. By studying dilute Cu(Au) surfaces under reactive conditions, we bridge the atomic-scale structural and compositional transformations driven by the high mobility of noble atoms between surface and subsurface layers.

The interplay between gas-surface reactions and dynamic segregation revealed here holds broad relevance for alloy systems, as most engineered materials—whether by design or through inherent impurities—are multicomponent. Under reactive conditions, the partitioning of alloying elements (or impurities) between surface and subsurface regions is ubiquitous, dictated by their relative chemical affinities and environmental stimuli. Our findings provide atomistic insights for understanding such dynamic surface reconfiguration, with immediate implications for materials design. For instance, corrosion-resistant coatings could exploit noble metal mobility to self-stabilize under oxidative stress, while metastable nanostructures with stimuli-responsive catalytic sites might be engineered by tailoring element-specific segregation energetics.

Our in-situ experiments are conducted using an aberration-corrected environmental TEM equipped with a differential pumping system. This setup allows for higher gas pressure in the sample region while maintaining a high vacuum throughout the rest of the TEM column. For our in-situ TEM experiments, we employ Cu-10at.%Au ($Cu_{90}Au_{10}$) thin film samples with a nominal thickness of ~500 Å. The experimental procedure begins with in-situ preparation of oxide-free surfaces. This involves annealing the $Cu_{90}Au_{10}$ film at 350°C in a H_2 atmosphere to induce faceted crack and tears, similar to the mechanical cleavage of crystals in vacuum for surface science experiments, resulting in atomically pristine surfaces. Subsequently, the gas flow is switched to O_2 gas flow to induce dissociative O_2 adsorption and oxide formation along these surface facets. Further experimental details can be found in the Supplemental Information.

Fig. 1 presents in-situ high-resolution (HR) TEM images that capture the dynamic evolution of the (110) surface of the $Cu_{90}Au_{10}$, viewed edge-on along the [001] zone axis, during exposure to 5×10^{-6} Torr O_2 and at 450°C. In Fig. 1(a), the surface displays a stepped morphology, comprising atomically flat (110) terraces separated by monoatomic steps. The in-situ observations clearly illustrate the transformation of the flat surface into a wave-like hill-and-valley configuration, with the undulations propagating laterally across the surface toward the un-oxidized surface region. For the pristine Cu(110) surface, the close-packed direction is along the [110] direction, characterized by a lattice periodicity of 2.5 Å. The observed ~2.5 Å periodicity in the un-oxidized region confirms that the (110) surface maintains the intact bulk-terminated structure before its transformation into the oxygenated undulation morphology. Notably, the emergence of the surface undulations represents a significant departure from dissociative O_2 adsorption on pure Cu(110), which typically results in either (2×1) or (6×2) reconstructions with surface periodicities of 5 Å and 7.5 Å, respectively[18-29]. This difference underscores the pronounced effect of alloyed

Au in inducing the resulting undulation of the oxygenated surface, where the atom columns in the topmost layer correspond to Cu-O chains whereas the atoms in the second layer correspond to Au-rich columns. Both exhibit brighter image contrast, as shown later by DFT modeling and HRTEM image simulations. Furthermore, as evident in Figs. 1(a-f), the atom columns—some marked by yellow arrows—display slightly brighter image contrast, suggesting Au enrichment in the topmost surface layer of the un-oxidized terrace regions.

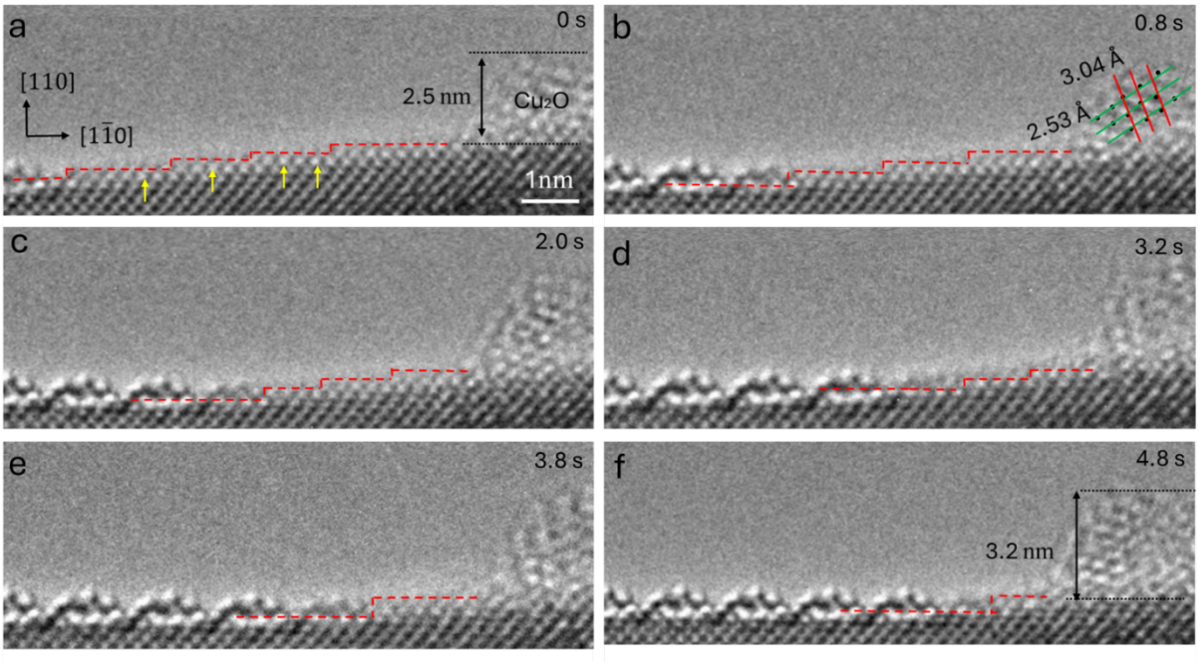

Figure 1: In-situ HRTEM imaging of the dynamic transformation of a flat (1×1) $Cu_{90}Au_{10}$(110) surface into a hill-and-valley oxygenated overlayer at 450°C and 5×10^{-6} Torr O_2. (a-f) Time-lapsed HRTEM images extracted from Supplementary in-situ TEM video 1. The red dashed lines outline the step-terrace morphology of the unoxidized terraces in front of the growth front of an undulated oxide overlayer. Yellow arrows mark some atom columns that exhibit brighter image contrast, indicating Au enrichment in the topmost layer of the un-oxidized terraces.

The in-situ HRTEM imaging in Figs. 1(a-f) also reveals that the lateral growth of the undulated oxide overlayer occurs via direct conversion of the topmost atomic layer of the metal substrate into the oxide. This conversion is evidenced by the reduced surface height of the oxide/metal interface compared to the unoxidized terrace in front of the undulated oxide overlayer. The red dashed lines in Fig. 1(a-f) outline the stepped feature of the oxide growth front in relation

to the unoxidized terrace and highlight the height difference between the oxide/metal interface and the unoxidized terrace. This step-flow solid-solid transformation happens as adsorbed O reacts directly with the substrate Cu atoms at the oxide growth front. Notably, this process does not require long-range diffusion of Cu adatoms to reach the growth front of the undulated oxide overlayer, as demonstrated by the consistent monoatomic step height of the oxide growth front. This consistent step height leads to the formation of an atomically flat interface between the substrate and undulated oxide layer, despite the stepped structure of the unoxidized terraces. During this transformation, the surface steps on the unoxidized terraces exhibit some receding motion, resulting in the formation of Cu adatoms detaching from the step edges and being captured by the growing oxide island in the top-right corner region of the surface. The measured lattice spacings of ~2.5 Å and ~3.0 Å for the oxide island match the (111) and (110) interplanar spacings of Cu_2O, respectively. The in-situ TEM imaging shows the progressive growth of the Cu_2O island over time, as indicated by its increasing surface height from ~2.5 nm in Fig. 1(a) to ~3.2 nm in Fig. 1(f). The growth of the Cu_2O island involves capturing mobile Cu adatoms form the surrounding unoxidized surface area. This process reduces surface diffusion of Cu adatoms generated from the receding surface steps to the growth front of the undulated oxide overlayer, thereby facilitating the solid-solid transformation of the flat metal surface to the undulated oxide layer. The transformation of the flat (110) surface into the hill-and-valley undulation is observed across various surface regions and samples of the $Cu_{90}Au_{10}$(110), as shown in Fig. S1.

Fig. 2 presents in-situ HRTEM images that reveal the dynamic transitions between the hill-and-valley configuration and a relatively flattened surface morphology of the oxide overlayer. As marked in Fig. 2(a), the atom columns at the peak positions of the undulated oxide overlayer exhibit a lateral periodicity of ~ 12.9 Å and a surface height of ~ 3.8 Å. In contrast, the atom

columns located at the valley positions show a reduced surface height of ~ 2.1 Å. Subsequently, Figs. 2(b-d) show the gradual flattening of the oxide overlayer, evident by the downward displacement of the atom columns at the peak positions. The surface heights decrease to 3.5 Å, 2.8 Å, and eventually converge to a relatively uniform height of 2.6 Å across all the bright atom columns within the topmost layer. Additionally, the atom columns at the original valley positions (marked by the yellow dashed lines in Figs. 2(a, d)) maintain a relatively weaker image contrast and show a slightly lower surface height of ~2.4 Å in the flattened configuration. The flattening process takes ~ 2.2 s to complete and occurs simultaneously across the entire surface, with all atom columns at the peak positions moving downward concurrently. This synchronized movement indicates similar stability among the atom columns. The homogeneous transition from the hill-and-valley surface configuration to the flattened morphology requires coordinated collective movement of all the atoms across the entire surface within the field of view. This contrasts with the lateral growth of the undulated oxide overlayer observed in Fig. 1, where the step-flow solid-solid transformation is highly confined to the substrate atoms local to the oxide growth front.

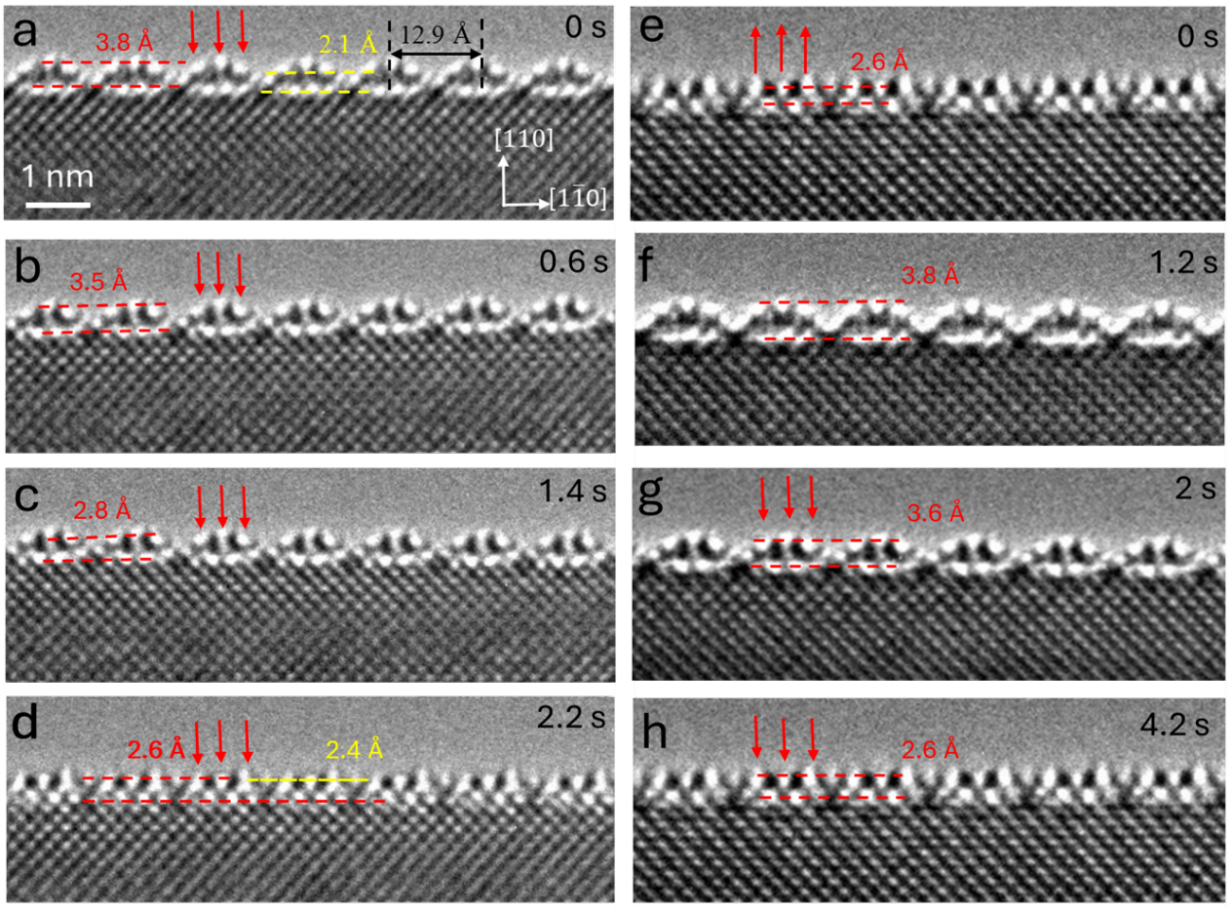

Figure 2: In-situ HRTEM imaging of the interconversion between surface undulating and flattening of $Cu_{90}Au_{10}$(110) at 450°C and ~5×10^{-6} Torr O_2. (a-d) Transformation from the undulated surface to a flattened surface (Supplementary in-situ TEM video 3). (e-h) Interconversion between the undulated and flattened surface configurations (Supplementary in-situ TEM video 4).

Figs. 2(e-h) demonstrate that the flattening process is reversible, resulting in the restoration of the hill-and-valley surface configuration. As shown in Fig. 2(e), the atom columns in the topmost layer of the oxide overlayer have a surface height of ~ 2.6 Å. The atom columns marked by the red arrows are observed to move upward concurrently, stabilizing at the surface height of ~ 3.8 Å (Figs. 2(f, g)), which results in the reformation of the hill-and-valley morphology within ~ 2 s. Following this, the undulated oxide overlayer undergoes another flattening cycle (Figs. 2(f-h)), with a duration of 1.8 s, similar to the flattening process shown in Figs. 2(a-d). The in-situ

TEM imaging confirms the synchronized movement of the atoms across the entire surface during the repeated interconversion between the undulated and flattened morphologies.

The in-situ TEM imaging presented above reveals a significant difference in surface oxidation behavior between $Cu_{90}Au_{10}$ and pure Cu. Specifically, the $Cu_{90}Au_{10}(110)$ surface exhibits a wavy-like undulation morphology upon dissociative O_2 adsorption, contrasting with the well-established (2×1) or (6×2) reconstructions typically observed for pure Cu(110)[21, 23, 24, 27, 30]. This difference can be attributed to the interfacial Au segregation induced by O_2 exposure. On the pristine surface of $Cu_{90}Au_{10}(110)$ (i.e., under H_2 annealing), Au atoms segregate to the surface due to the lower surface energy and larger atomic size of Au compared to Cu[31-33]. This Au surface enrichment is evident from the slightly brighter image contrast of atom columns in the topmost surface layer of the unoxidized terraces, as shown in Fig. 1. However, when exposed to an oxidizing atmosphere, O_2 adsorption promotes Cu segregation to the surface. This occurs because Cu has a higher affinity for O, which compensates for its higher surface energy relative to Au, leading to surface oxidation of Cu and inward migration of Au from the topmost surface layer to the subsurface. This shift in surface composition upon O_2 exposure aligns with reported ambient-pressure X-ray photoelectron spectroscopy measurements of surface composition evolution of $Cu_3Au(100)$ when transitioning from H_2 to O_2 atmospheres[34, 35]. The evolution of image contrast in the atom columns observed in our in-situ HRTEM imaging highlights the critical role of subsurface Au enrichment in driving surface undulations upon O_2 adsorption.

The atomic mechanisms underlying the observed surface undulation shown in Fig. 1, as well as the interconversion between the undulated and flattened surface configurations of the oxide overlayer shown in Fig. 2 are elucidated through DFT modeling. Fig. 3(a) displays a zoomed-in HRTEM of the oxidized $Cu_{90}Au_{10}(110)$, revealing an amplitude of ~ 3.8 Å and a peak-to-peak

188 spacing of ~12.9 Å of the surface undulation, with hills and valleys parallel to the [001] direction
189 of the (110) surface. This undulation wavelength matches 5 [$1\bar{1}0$]-(1×1) lattice spacings of the
190 (110) substrate. The arrangement of atom columns in the topmost surface layer differs from that
191 in the substrate, featuring three bright atom columns (marked by the red arrows) within the hill
192 region and two slightly dimmed atom columns (marked by the blue arrows) in the valley region.
193 Additionally, as depicted in Fig. 3(a), the two interfacial atom columns (marked by the purple
194 arrows) beneath the hill region exhibit a strongly bright image contrast. In contrast, the two
195 adjacent interfacial atom columns (marked by the blue arrows) show relatively dim image contrast,
196 while the atom column right beneath the valley region (marked by red dotted circle) appears much
197 dimmed. Furthermore, the three atom columns (also marked by dotted circles) situated within the
198 hill region display significantly dimmed image intensity. These variations in image intensity
199 among the interfacial atom columns suggest differences in their Au contents, resulting from O
200 adsorption-induced inward segregation of Au from the topmost surface to various interfacial sites
201 of the substrate.

202 Based on the image intensity analysis of the experimental HRTEM observations presented
203 in Fig. 3(a), we construct a structural model of the undulated oxide overlayer. This model
204 incorporates the solid-solid transformation of the segregated topmost Cu atoms into Cu-O-Cu
205 chains, along with the interfacial injection of Au atoms from the topmost layer. Fig. 3(b) illustrates
206 the DFT-obtained minimum-energy structure, depicting the resulting hill-and-valley surface
207 configuration. In this configuration, the topmost three atom columns of the hill region correspond
208 to Cu-O-Cu chains (indicated by the red arrows). In contrast, the two atom columns in the valley
209 region, marked by the blue arrows, consist of 50%Au ($Cu_{50}Au_{50}$). The three atom columns in the
210 second layer of the hill region—two by red dotted circles and one by a green dotted circle directly

beneath the peak position—correspond to two full Cu columns and one Cu column containing 50% vacancies ($Cu_{50}Vac_{50}$), respectively. The two atom columns in the third layer (indicated by the purple arrows) of the hill region are composed of pure Au, while the adjacent atom columns, marked by the blue arrows, have a composition of $Cu_{50}Au_{50}$. The atom column directly beneath the valley region corresponds to pure Cu, as indicated by the red dotted circle. The DFT-relaxed structure shows an amplitude of ~ 3.6 Å for the Cu-O-Cu chain at its peak and a peak-to-peak periodicity of ~13 Å, which closely align with the values observed in the experimental HRTEM image (Fig. 2(a)).

Fig. 3(c) presents the simulated HRTEM image based on the DFT-relaxed structure depicted in Fig. 3(b). It closely matches all the key features of the experimental HRTEM image, including the amplitude and wavelength of the surface undulation, as well as the image contrast of the individual atom columns. Notably, this encompasses the strongest image contrast observed for the three Cu-O-Cu chains of the hill region and the two pure interfacial Au columns under the hill region. Additionally, relatively dimmed image intensity is observed for the interfacial $Cu_{50}Au_{50}$ atom columns, while significantly dimmed image intensity for the pure Cu columns.

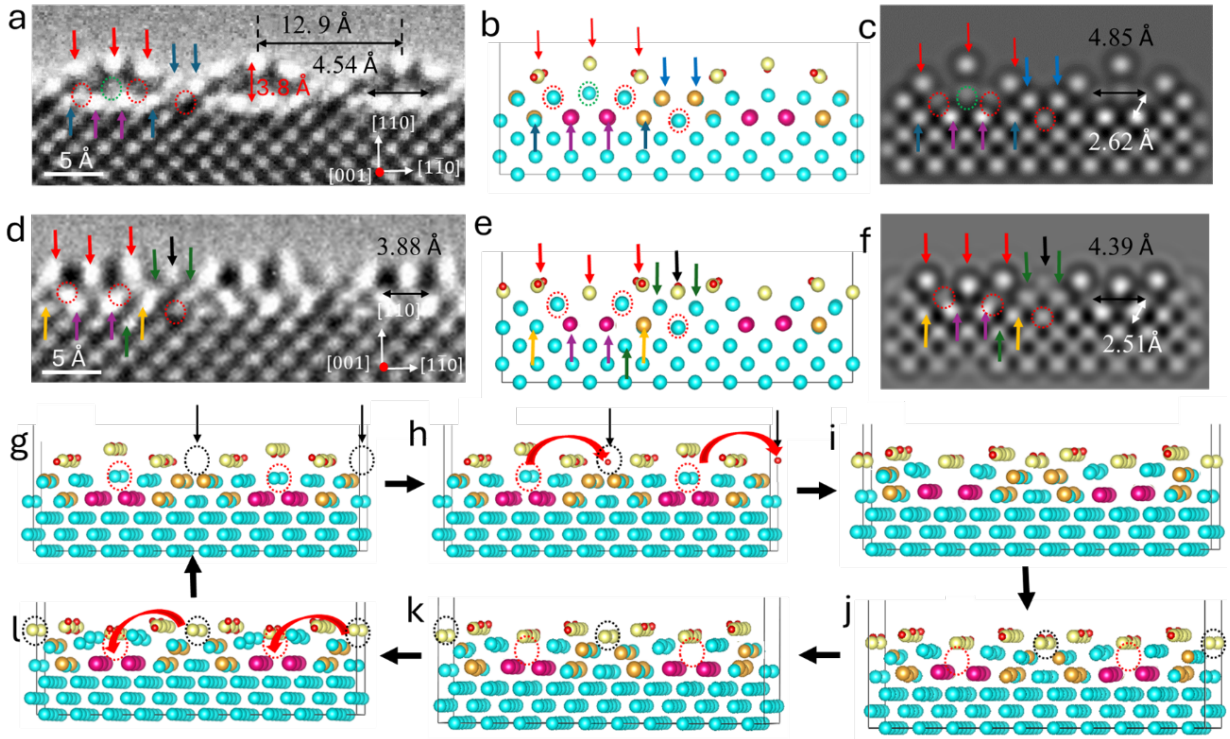

Figure 3: DFT modeling of the interconversion between undulated and flattened surface configurations of the oxide overlayer on $Cu_{90}Au_{10}$(110). Experimental and simulated HRTEM images, along with DFT-relaxed structure models for both the undulated (a-c) and flattened oxide overlayer (d-f), respectively. The red arrows denote Cu-O-Cu atom columns, black arrows for Cu-O-Cu columns with 50% O vacancies, purple arrows for pure Au columns, blue arrows for $Cu_{50}Au_{50}$ columns, green arrows for $Cu_{75}Au_{25}$ columns, yellow arrows for $Cu_{25}Au_{75}$ columns, red dotted circles for pure Cu atom columns, and green dotted circles for Cu columns with 50% vacancies. (g-l) DFT-derived atomic processes leading to one cycle of transformations between undulation, flattening, and back to undulation of the oxide overlayer.

Fig. 3(d) displays an enlarged HRTEM image of the flattened surface configuration of the oxide overlayer, featuring three bright atom columns (marked by red arrows) and one dimmed atom column (marked with a black arrow) within each periodicity. The second layer consists of atom columns with relative dimmed image contrast (identified by red dotted circles and blue arrows). The third layer contains the two strong intensity columns (highlighted by the purple arrows), two dimmer atom columns (noted with yellow arrows), and one dimmest atom (marked by the red dotted circle). Based on the arrangement of the atom columns and their image intensities in the HRTEM image, we construct a structural model (Fig. 3(e)) for the flattened surface. Here,

the topmost layer consists of three Cu-O-Cu chains and one Cu-O-Cu chain with 50% O vacancies, as marked by the red arrows and black arrow in Fig. 3(f), respectively. Contrasting with the undulated surface model (Fig. 3(b)), the Cu atom column in the second layer directly below the peak atom column is now entirely vacant, facilitating the downward relaxation of the peak Cu-O-Cu column for the formation of the flattened structure. In contrast, the image intensity of the atom columns (marked by the green arrows in Fig. 3(d)) in the second layer of the original valley region become dimmed.

Fig. 3(e) illustrates the DFT-obtained minimum energy structure, revealing the downward relaxation of the atom columns in the topmost layer to result in the flattened surface configuration. Unlike the undulated surface (Fig. 3(b)), the flattened oxide layer features three Cu-O-Cu chains and an additional Cu-O-Cu chain with 50% O vacancies (highlighted by the black arrow) within each periodicity of the topmost layer. This configuration indicates a higher O coverage for the flattened surface, which may drive the inward migration of some Au atoms from the second and third layers of the original undulated surface to deeper layers. This phenomenon is observable in the HRTEM image in Fig. 3(d), where certain atom columns (as marked by the yellow arrows) in the third exhibit enhanced image contrast compared to those in Fig. 3(a), due to the enrichment of Au atoms toward deeper layers. The Au enrichment also occurs in the fourth layer, resulting in some originally dark intensity columns transforming into brighter intensity columns ($Cu_{75}Au_{25}$), as indicated by the green arrows in Fig. 3(d).

Fig. 3(f) presents a simulated HRTEM image using the DFT-relaxed structure depicted in Fig. 3(e). It closely mirrors the essential features observed in the experimental HRTEM image, including the arrangement and image contrast of the atom columns. Specifically, the simulated image replicates distinct characteristics observed in the experimental data, such as the pronounced

image contrast for the three Cu-O-Cu chains and pure Au columns as well as the relatively dimmed image contrast for the Cu-O-Cu chains with 50% O vacancies. Furthermore, it captures the diminished image intensity for the $Cu_{75}Au_{25}$ atom columns in the second layer and notably weaker image intensity for the pure Cu atom column (red dotted circle) in the third layer. As shown in Fig. 3(d), the pure Cu atom columns in the second layer and the pure Au atom columns in the third layer shift toward each other upon surface flattening, as evidenced by the reduction in the Cu-Au distance between the two layers from 2.61 Å in the undulated oxide layer (Fig. 3(a)) to 2.52 Å in the flattened oxide layer. This suggests that as the undulated surface flattens, the Cu-Au bonds shorten, which leads to the slightly overlapping of the image contrast of the atom columns in the HRTEM image. Our in-situ HRTEM imaging further shows that this flattening process reduces the distance between adjacent pure Cu columns in the second layer from 4.54 Å to 3.88 Å. Similarly, our DFT results (Fig. 3(e)) exhibit a comparable trend, with the Cu-Cu distance decreasing from 4.85 Å to 4.39 Å.

It is worth noting that the circled atomic columns in the undulated (Fig. 3a) and flattened (Fig. 3d) regions show slight contrast differences, suggesting apparent asymmetry. These variations may arise from local compositional differences or imaging artifacts due to slight off-zone-axis orientation. DFT calculations, performed by systematically varying the column compositions, show that the symmetric configurations (Figs. 3b and 3e)) consistently yield the lowest total energy, indicating the symmetrical configurations are the most stable—consistent with the experimentally observed persistence of both surface structures. Additionally, HRTEM simulations with varying tilt angles (Fig. S2) reveal that small tilts can introduce asymmetry in contrast between otherwise equivalent columns. Together, these results suggest that the observed asymmetries are likely imaging artifacts rather than intrinsic structural features.

The microscopic processes underlying the formation of the undulated surface configuration and its reversible transformation to the flattened morphology are further elucidated through the atomistic modeling. As demonstrated by the in-situ HRTEM imaging in Fig. 1, the genesis of the hill-and-valley surface undulation is induced by dissociative O_2 adsorption, which transforms the Cu atoms in the topmost layer into Cu-O-Cu chains and prompts the inward segregation of Au atoms from the topmost surface into inner layers. Through DFT calculations of the Au segregation energies, we pinpoint the most favorable locations for inward Au segregation when the surface is covered with Cu-O-Cu chains. These locations reside in the third layer underneath the hill region, with the segregation energies of -0.42 eV and -0.27 eV (Fig. S3 and Table S1), resulting in the formation of pure Au and $Cu_{50}Au_{50}$ columns. Similarly, sites in the second layer directly beneath the valley region are found to be less favorable, but they still exhibit a negative Au segregation energy of -0.24 eV, hence these atom columns are expected to contain 50% Au (i.e., $Cu_{50}Au_{50}$ atom columns as well), consistent with their relatively weaker image intensity compared to the pure Au atom columns observed in the HRTEM image. Segregation of Au to any other sites in the second and third atomic layers yields a positive segregation energy, rendering them unfavorable for Au adsorption. Therefore, Au segregation to these favorable lattice sites results in the undulated surface configuration depicted in Fig. 3(b).

Figs. 3(g-i) delineates the DFT-derived atomic process driving the transformation from the undulated surface configuration (Fig. 3(b)) to the flattened morphology (Fig. 3(e)). As previously elucidated, achieving surface flattening requires the creation of a vacant atom column directly beneath the hill Cu-O-Cu column, allowing for the downward relaxation of the peak Cu-O-Cu column. Simultaneously, the flattening process entails the formation of a new atom column in the valley region, as indicated by the black dotted circles in Fig. 3(g). Relocating the second-layer Cu

atom column directly beneath the peak column, which contains 50% vacancies and is denoted by the dotted red circle, to the location marked by the black arrow (the black dotted circle) in Fig. 3(h) would result in the creation of a completely vacant column directly beneath the peak Cu-O-Cu column. This shift would also result in the emergence of a new Cu column with 50% vacancies in the valley region. However, this alternation proves to be energetically unfavorable, resulting in a higher system energy by 0.59 eV. Nonetheless, the introduction of a new Cu column at the outermost surface renders it conducive to O adsorption, with an O adsorption energy of -1.72 eV. The conversion of this Cu column into a Cu-O-Cu chain (with 50% O vacancies) leads to a significant reduction in system energy by 1.42 eV. Therefore, the surface flattening process involves the downward movement of the peak Cu-O-Cu chain toward the vacant column, along with the formation of a new Cu-O-Cu chain in the valley region. This leads to a slight increase in the surface height of the valley region, consistent with the in-situ HRTEM imaging shown in Figs. 2(a-d), which shows that the surface flattening is accompanied by a small height increase in the valley region from 2.1 Å in the undulated structure to 2.4 Å in the flattened surface. A key step in this process is the migration of the second-layer Cu atom (indicated by the red dotted circle) beneath the peak Cu-O-Cu chain to the surface valley region, as marked by the red curve arrow in Fig. 3(h). The formation of the Cu-O-Cu chain in the valley region renders the Au atoms beneath in the second layer unstable, driving their inward segregation to deeper layers. As illustrated in Fig. 3(i), Au tends to segregate to the third layer, increasing the percentage of Au from $Cu_{50}Au_{50}$ to $Cu_{25}Au_{75}$, with a segregation energy of -0.43 eV. This results in the ultimate configuration of the flattened structure depicted in Fig. 3(j).

Figs. 3(j-k) illustrate the reverse process leading to the restoration of the valley-and-hill undulation from the flattened structure. This process begins with the desorption of O from the

newly formed Cu-O-Cu chain that contains 50% O vacancies (i.e., the atom column marked by the black dotted circle in Fig. 3(j)), making it less stable than the oxygenated Cu-O-Cu chains. This desorption results in freed Cu adatoms that become unstable on the surface. The subsurface sites in the second atomic layer, as marked by the red dotted circles in Fig. 3(k), are identified as the most stable locations for these Cu adatoms to reside. The migration of the Cu adatoms to these stable subsurface sites leads to a lowered system energy by -0.76 eV. This drives the upward relaxation of the Cu-O-Cu chain right above the newly added Cu atom column, resulting in the restoration of the surface undulation. Simultaneously, the sites directly below the valley region become favorable again for the outward segregation of Au from the third layer, with a segregation energy of -0.26 eV (Fig. 3(l)). This leads to the fully recovered hill-and-valley configuration shown in Fig. 3(g).

The DFT modeling presented above elucidates that the flattened surface exhibits a higher O coverage compared to the undulated surface configuration due to the formation of additional Cu-O-Cu chains in the valley regions of the surface. The experimentally observed reversible transitions between the undulated and flattened surface configurations (Fig. 2) are primarily attributed to the metastability of these additional Cu-O-Cu chains, which contain 50% Cu vacancies and are thus less stable than the fully intact Cu-O-Cu chains. Small fluctuations in O_2 pressure can induce O adsorption and desorption at the valley regions, thus facilitating the reversible transitions between the two surface configurations.

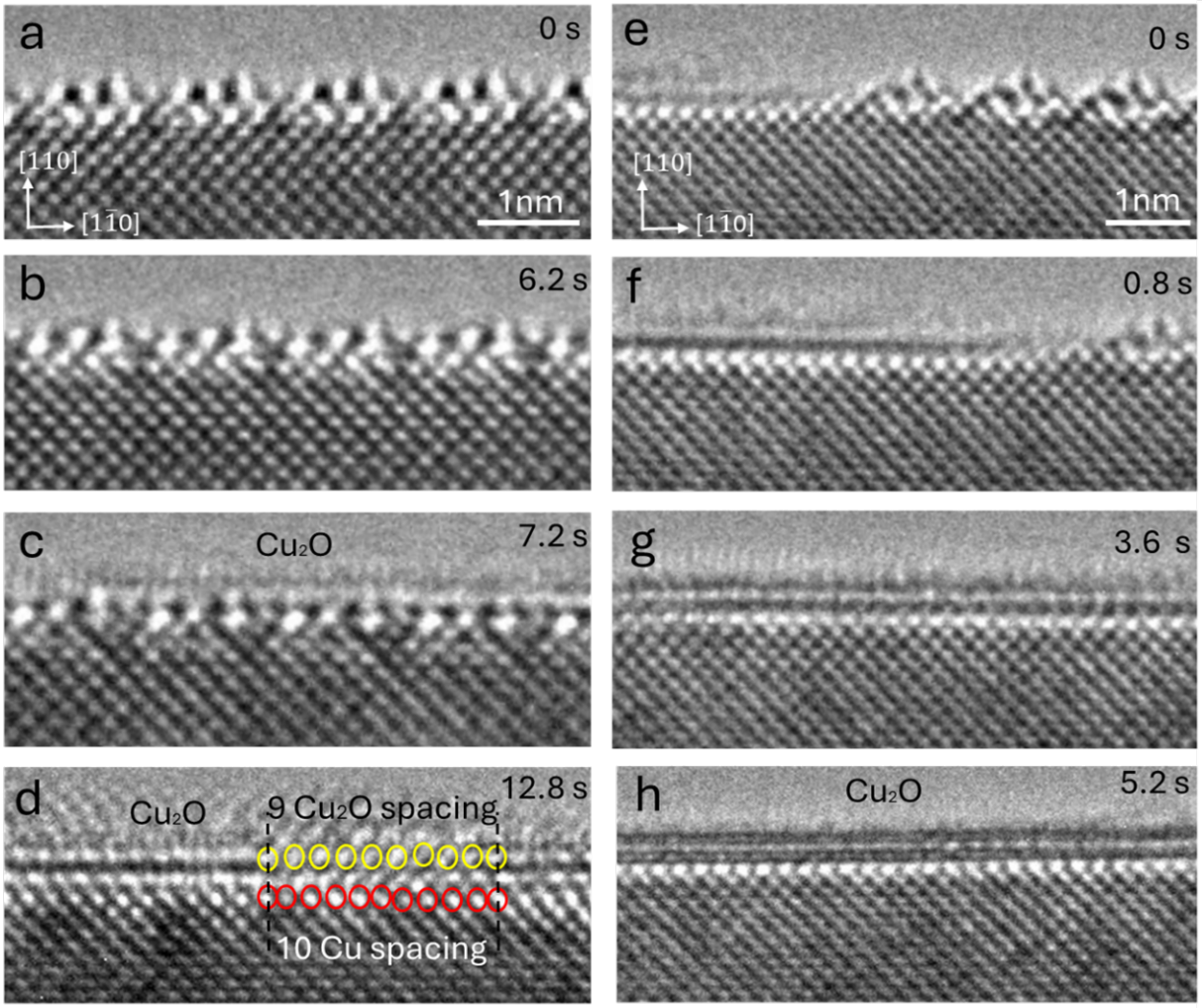

Figure 4: (a-d) In-situ HRTEM images (Supplementary in-situ TEM video 5) showing the transformation from the flattened surface configuration to a Cu_2O overlayer on $Cu_{90}Au_{10}(110)$ at 450°C and 5×10^{-6} Torr O_2. (e-h) In-situ HRTEM images (Supplementary in-situ TEM video 6) depicting the direct conversion from the undulated surface to the Cu_2O overlayer at 450°C and 1×10^{-5} Torr O_2. The significantly enhanced image intensity of the atom columns beneath the oxide layer is due to the oxidation-induced interfacial enrichment of Au.

Logically, a higher O_2 pressure would favor the stabilization of Cu-O-Cu chains in the valley regions by promoting O adsorption, whereas a decrease in O_2 pressure would have the opposite effect. This expectation is confirmed experimentally through in-situ HRTEM observations. As depicted in Figs. 4(a-d), a slight increase in O_2 pressure to 5×10^{-6} Torr not only drives the transformation of the undulated surface into the flattened surface morphology but also

367 further oxidizes the flattened surface into a thin Cu_2O-like layer with the lattice spacing ~ 2.9 Å
368 and a (10×9) interfacial configuration with the (110) substrate (Fig. 4(d)). Figs. 4(e-h) illustrate
369 another sequence of HRTEM images showing the effect of O_2 exposure at a higher pressure of
370 1×10^{-5} Torr. These in-situ images demonstrate the direct oxidation of the undulated configuration
371 into a thin layer of Cu_2O, formed by the lateral growth of the Cu_2O overlayer toward the undulated
372 hill-and-valley region on the right. This solid-solid transformation of the undulated surface layer
373 into the Cu_2O overlayer bypasses the formation of the metastable, flattened surface configuration.
374 As shown in Figs. 4(d, h), the substrate atom columns beneath the Cu_2O overlayer exhibit a
375 significantly enhanced image contrast, indicating substantial Au enrichment due to the interfacial
376 injection of Au atoms from the oxidized surface region.

377 Using first-principles thermodynamic analysis based on DFT calculations (details in
378 Supporting Information), we estimate the equilibrium O_2 pressure for the reversible transition
379 between undulated and flattened surface morphologies to be $\sim10^{-11}$ Torr at 450 °C (Fig. S4).
380 However, our in-situ TEM observations reveal that these structural transitions occur at
381 significantly higher O_2 pressure—between 1×10^{-6} to 1×10^{-5} Torr at 450 °C (Figs. 2, 4), roughly
382 five orders of magnitude above the thermodynamic prediction.

383 This discrepancy is likely from kinetic hindrance, a known factor that often shifts
384 experimental transition thresholds far above equilibrium values[23, 25, 36-39]. As shown in our NEB
385 calculations (Figs. S5 and S6), the phase transitions require substantial diffusion of Cu and Au
386 atoms between the surface and subsurface, with energy barriers ranging from 0.69 to 0.86 eV.
387 Although the energy barriers are not prohibitively high, the kinetic complexity of the transition
388 pathway—especially under dynamic in-situ conditions—requires higher O_2 pressures to be
389 realized experimentally. Additionally, these transitions also accompanied by energetically

favorable restructuring, where flattening (induced by O adsorption) promotes Cu migration to the surface and Au incorporation into the subsurface, lowering the system energy by ~1.85 eV, whereas undulation (induced by O desorption) reverses this exchange, lowering energy by ~1.12 eV. These results support the conclusion that, although the equilibrium pressure is extremely low, thermal activation and kinetic barriers shift the actual transition threshold to much higher O_2 pressures under experimental conditions.

It is worth noting that, due to variations in gas dosing dynamics and the frame rate limitations of our current imaging setup, we were unable to extract consistent transition frequencies or determine the precise periodicity of the surface transformations shown in Figs. 2 and 4. Future studies employing higher frame rate imaging and more precisely controlled gas delivery systems will be important for quantitatively correlating transition rates with O_2 pressure and temperature. Such improvements will enable a more detailed understanding and control of the surface dynamics.

The results presented here provide mechanistic insights into how atomic-scale surface dynamics in alloys are governed by the interplay between reactive environments and atomic-level element distribution. By revealing the oxygen-driven, cyclic segregation-disegregation of Au in Cu(Au)—a process that dynamically reconfigures the surface into high-and-valley morphologies—we demonstrate how atomic-scale chemical activity contrasts govern the evolution of surface structure and composition. The observed atomic-scale feedback loop, where oxygen adsorption and desorption trigger reversible Au redistribution between surface and subsurface regions, enables adaptive surface restructuring in alloys under reactive conditions. These findings have broad implications for the engineering of alloys that dynamically optimize their structure and composition in response to environmental stimuli. Practically, this could lead to the rational design

of corrosion-resistant coatings that self-reconfigure to passivate against reactive gases, as well as catalytic nanostructures with tunable active sites by leveraging controlled surface-subsurface exchange. Furthermore, the ability to stabilize metastable morphologies through nanoscale feedback mechanisms opens avenues for tuning surface properties, bridging atomic-scale segregation dynamics to functional performance in catalysis and environmental applications.

In-situ TEM imaging of the surface oxidation of Cu(Au) reveals a solid-solid transformation of the topmost atomic layer, evolving into a hill-and-valley undulation with reversible interconversion between undulated and flattened surface states. Coordinated DFT modeling provides insight into the microscopic process driving these interconversions and identifies the metastability of surface flattening during the oxidation pathway leading to Cu_2O formation. The observed surface dynamics are driven by fluctuations in O_2 pressure fluctuations, where O adsorption occurs at higher pressures, while O desorption takes place at lower pressures. These fluctuations induce the desegregation and segregation of Au atoms between the topmost surface layer and subsurface lattice sites, resulting in dynamic changes in the atomic structure and composition of the surface. These in-situ atomic-scale observations offer a detailed understanding of the dynamic evolution of the surface and subsurface in Cu-Au alloys under varying environmental conditions. The mechanistic insights gained from this study have broader implications for other alloy systems, where differences in the chemical activity of alloying elements lead to surface segregation and oxidation of the reactive metal, along with subsurface desegregation of the more noble metal. These opposing processes of segregation and desegregation significantly influence the dynamic evolution of surface structure, composition, and properties—key factors in technological applications such as heterogeneous catalysis. In such systems, fluctuations in gas pressures or the presence of co-existing oxidizing and reducing gases can trigger

similar atomic-scale dynamics in both the surface and subsurface regions of multicomponent catalysts.

Supporting Information

Experimental and computation methods; Figures S1-S6; Tables S1; Captions for supplementary in-situ TEM movies 1-6

Acknowledgements

This work was supported by the US Department of Energy, Office of Basic Energy Sciences, Division of Materials Sciences and Engineering under award number DE-SC0001135. This research used the resources of the Environmental TEM Catalysis Consortium (ECC), which is supported by the University of Pittsburgh and Hitachi High Technologies. Additionally, this research used the Theory and Computation resources of the Center for Functional Nanomaterials at Brookhaven National Laboratory, which is supported by the US Department of Energy, Office of Basic Energy Sciences, under contract number DE-SC0012704.

Competing financial interests: The authors declare no competing financial interests.

References:

1. Raabe, D.; Herbig, M.; Sandlöbes, S.; Li, Y.; Tytko, D.; Kuzmina, M.; Ponge, D.; Choi, P.-P., Grain Boundary Segregation Engineering in Metallic Alloys: A Pathway to the Design of Interfaces. *Curr. Opin. Solid State Mater. Sci.* **2014,** *18*, 253-261.
2. Zafeiratos, S.; Piccinin, S.; Teschner, D., Alloys in Catalysis: Phase Separation and Surface Segregation Phenomena. *Catal. Sci. Technol.* **2012,** *2*, 1787-1801.
3. Pielsticker, L.; Zegkinoglou, I.; Han, Z.-K.; Navarro, J. J.; Kunze, S.; Karslıoğlu, O.; Levchenko, S. V.; Roldan Cuenya, B., Crystallographic Orientation Dependence of Surface Segregation and Alloying on PdCu Catalysts for CO2 Hydrogenation. *J. Phys. Chem. Lett.* **2021,** *12* (10), 2570-2575.
4. Pia, G.; Sogne, E.; Falqui, A.; Delogu, F., Ag Surface Segregation in Nanoporous Au Catalysts During CO Oxidation. *Sci. Rep.* **2018,** *8*, 15208.
5. Breyton, G.; Amara, H.; Nelayah, J.; Creuze, J.; Guesmi, H.; Alloyeau, D.; Wang, G.; Ricolleau, C., Atomic-Scale Surface Segregation in Copper-Gold Nanoparticles. *Phys. Rev. Lett.* **2023,** *130* (23), 236201.
6. Chao, H.-Y.; Venkatraman, K.; Moniri, S.; Jiang, Y.; Tang, X.; Dai, S.; Gao, W.; Miao, J.; Chi, M., In Situ and Emerging Transmission Electron Microscopy for Catalysis Research. *Chem. Rev.* **2023,** *123* (13), 8347-8394.
7. Chi, M. F.; Wang, C.; Lei, Y. K.; Wang, G. F.; Li, D. G.; More, K. L.; Lupini, A.; Allard, L. F.; Markovic, N. M.; Stamenkovic, V. R., Surface Faceting and Elemental Diffusion Behaviour at Atomic Scale for Alloy Nanoparticles During in Situ Annealing. *Nat. Commun.* **2015,** *6*, 8925.
8. Zou, L. F.; Yang, C. M.; Lei, Y. K.; Zakharov, D.; Wiezorek, J. M. K.; Su, D.; Yin, Q. Y.; Li, J.; Liu, Z. Y.; Stach, E. A.; Yang, J. C.; Qi, L.; Wang, G. F.; Zhou, G. W., Dislocation Nucleation Facilitated through Atomic Segregation. *Nat. Mater.* **2018,** *17*, 56-63.
9. Li, X.; Cheng, S.; He, Y.; Qian, L.; Zakharov, D.; Wu, G.; Shan, C.; Zhang, L.; Su, D., Revealing the Dynamics of the Alloying and Segregation of Pt-Co Nanoparticles via In-Situ Environmental Transmission Electron Microscopy. *Nano Res.* **2023,** *16* (2), 3055-3062.
10. Dai, S.; Hou, Y.; Onoue, M.; Zhang, S.; Gao, W.; Yan, X.; Graham, G. W.; Wu, R.; Pan, X., Revealing Surface Elemental Composition and Dynamic Processes Involved in Facet-Dependent Oxidation of Pt_3Co Nanoparticles via in Situ Transmission Electron Microscopy. *Nano Lett.* **2017,** *17* (8), 4683-4688.
11. Dai, S.; You, Y.; Zhang, S.; Cai, W.; Xu, M.; Xie, L.; Wu, R.; Graham, G. W.; Pan, X., In Situ Atomic-Scale Observation of Oxygen-Driven Core-Shell Formation in Pt_3Co Nanoparticles. *Nat. Commun.* **2017,** *8* (1), 204.
12. Dong, Z.; Nian, Y.; Liu, H.; Chen, J.; Wang, Y.; Wang, S.; Xu, J.; Han, Y.; Luo, L., Revealing Synergetic Structural Activation of a CuAu Surface During Water–Gas Shift Reaction. *Proc. Natl. Acad. Sci.* **2022,** *119* (23), e2120088119.
13. Fu, J.; Zhu, W.; Chen, Y.; Yin, Z.; Li, Y.; Liu, J.; Zhang, H.; Zhu, J.-J.; Sun, S., Bipyridine-Assisted Assembly of Au Nanoparticles on Cu Nanowires To Enhance the Electrochemical Reduction of CO_2. *Angew. Chem. Int. Ed.* **2019,** *58* (40), 14100-14103.
14. Guo, M.; Ma, P.; Wang, J.; Xu, H.; Zheng, K.; Cheng, D.; Liu, Y.; Guo, G.; Dai, H.; Duan, E.; Deng, J., Synergy in Au−CuO Janus Structure for Catalytic Isopropanol Oxidative Dehydrogenation to Acetone. *Angew. Chem. Int. Ed.* **2022,** *61* (27), e202203827.
15. Huang, J.; Dai, J.; Zhu, J.; Chen, R.; Fu, X.; Liu, H.; Li, G., Bimetallic Au-Cu Gradient Alloy for Electrochemical CO_2 Reduction into C_2H_4 at Low Overpotential. *J. Catal.* **2022,** *415*, 134-141.

16. Mosrati, J.; Ishida, T.; Mac, H.; Al-Yusufi, M.; Honma, T.; Parliniska-Wojtan, M.; Kobayashi, Y.; Klyushin, A.; Murayama, T.; Abdel-Mageed, A. M., Low-Temperature Hydrogenation of CO_2 to Methanol in Water on ZnO-Supported CuAu Nanoalloys. *Angew. Chem. Int. Ed.* **2023,** *62* (51), e202311340.
17. Tao, Z.; Wu, Z.; Yuan, X.; Wu, Y.; Wang, H., Copper–Gold Interactions Enhancing Formate Production from Electrochemical CO2 Reduction. *ACS Catal.* **2019,** *9* (12), 10894-10898.
18. Coulman, D. J.; Wintterlin, J.; Barth, J. V.; Ertl, G., An STM investigation of the Cu(110). *Surf. Sci.* **1990,** *240*, 151-162.
19. Coulman, D. J.; Wintterlin, J.; Behm, R. J.; Ertl, G., Novel Mechanism for the Formation of Chemisorption Phases: the (2×1)O-Cu(110) “Added-Row" Reconstruction. *Phys. Rev. Lett.* **1990,** *64*, 1761-1764.
20. Feidenhans, R.; Grey, F.; Nielsen, M.; Besenbacher, F.; Jensen, F.; Laegsgaard, E.; Stensgaard, I.; Jacobsen, K. W.; Norskov, J. K.; Johnson, R. L., Oxygen Chemisorption on Cu(110): a Model for the c(6x2) Structure. *Phys. Rev. Lett.* **1990,** *65* (16), 2027-2030.
21. Guillemot, L.; Bobrov, K., Morphological Instability of the Cu(110)–(2 × 1)–O Surface Under Thermal Annealing. *Phys. Rev. B* **2011,** *83* (7), 075409.
22. Li, L.; Cai, N.; Saidi, W. A.; Zhou, G. W., Role of Oxygen in Cu(110) Surface Restructuring in the Vicinity of Step Edges. *Chem. Phys. Lett.* **2014,** *613*, 64-69.
23. Li, L.; Liu, Q. Q.; Li, J.; Saidi, W. A.; Zhou, G. W., Kinetic Barriers of the Phase Transition in the Oxygen Chemisorbed Cu(110)-(2x1)-O as a Function of Oxygen Coverage. *J. Phys. Chem. C* **2014,** *118*, 20858-20866.
24. Li, L.; Zhou, G. W., Oxygen Subsurface Adsorption on the Cu(110)-c(6x2) Surface. *Surf. Sci.* **2013,** *615*, 57-64.
25. Liu, Q. Q.; Li, L.; Cai, N.; Saidi, W. A.; Zhou, G. W., Oxygen Chemisorption-Induced Surface Phase Transitions on Cu(110). *Surf. Sci.* **2014,** *627*, 75-84.
26. Wu, D. X.; Li, J.; Zhou, G. W., Oxygen Adsorption at Heterophase Boundaries of the Oxygenated Cu(110). *Surf. Sci.* **2017,** *666*, 28-43.
27. Wu, D. X.; Liu, Q. Q.; Li, J.; Sadowski, J. T.; Zhou, G. W., Visualizing Reversible Two-Dimensional Phase Transitions in Oxygen Chemisorbed Layers. *J. Phys. Chem. C* **2018,** *122*, 28233-28244.
28. Wu, D. X.; Sun, X. H.; Yang, J. C.; Zhou, G. W., Intermittent Oxidation Kinetics and Metal/Oxide Interfacial Undulation. *Phys. Rev. B* **2024,** *110*, 085402.
29. Wu, D. X.; Zhu, Y. G.; Shan, W. T.; Wang, J. Y.; Liu, Q. Q.; Zhou, G. W., Revealing an Intermediate Cu–O/OH Superstructure on Cu(110). *J. Phys. Chem. Lett.* **2022,** *13* (10), 2396-2403.
30. Li, M.; Curnan, M. T.; Saidi, W. A.; Yang, J. C., Uneven Oxidation and Surface Reconstructions on Stepped Cu(100) and Cu(110). *Nano Lett.* **2022,** *22* (3), 1075-1082.
31. Zou, L.; Saidi, W. A.; Lei, Y.; Liu, Z.; Li, J.; Li, L.; Zhu, Q.; Zakharov, D.; Stach, E. A.; Yang, J. C., Segregation Induced Order-Disorder Transition in Cu (Au) Surface Alloys. *Acta Mater.* **2018,** *154*, 220-227.
32. Zou, L.; Li, J.; Zakharov, D.; Saidi, W. A.; Stach, E. A.; Zhou, G., Atomically Visualizing Elemental Segregation-Induced Surface Alloying and Restructuring. *J. Phys. Chem. Lett.* **2017,** *8* (24), 6035-6040.
33. Tsuda, Y.; Oka, K.; Makino, T.; Okada, M.; Diño, W. A.; Hashinokuchi, M.; Yoshigoe, A.; Teraoka, Y.; Kasai, H., Initial Stages of Cu_3Au (111) Oxidation: Oxygen Induced Cu Segregation and the Protective Au Layer Profile. *Phys. Chem. Chem. Phys.* **2014,** *16* (8), 3815-3822.
34. Li, C. R.; Liu, Q. Q.; Boscoboinik, J. A.; Zhou, G. W., Tuning the Surface Composition of Cu_3Au Binary Alloy. *Phys. Chem. Chem. Phys.* **2020,** *22*, 3379-3389.
35. Li, J.; Zhang, S.; Li, C. R.; Zhu, Y. G.; Boscoboinik, J. A.; Tong, X.; Sadowski, J.; Wang, G. F.; Zhou, G. W., Coupling Between Bulk Thermal Defects and Surface Segregation Dynamics. *Phys. Rev. B* **2021,** *104*, 085408.

36. Lundgren, E.; Gustafson, J.; Mikkelsen, A.; Andersen, J. N.; Stierle, A.; Dosch, H.; Todorova, M.; Rogal, J.; Reuter, K.; Scheffler, M., Kinetic Hindrance During the Initial Oxidation of Pd(100) at Ambient Pressures. *Phys. Rev. Lett.* **2004,** *92* (4), 046101.
37. Westerstrom, R.; Gustafson, J.; Resta, A.; Mikkelsen, A.; Andersen, J. N.; Lundgren, E.; Seriani, N.; Mittendorfer, F.; Schmid, M.; Klikovits, J.; Varga, P.; Ackermann, M. D.; Frenken, J. W. M.; Kasper, N.; Stierle, A., Oxidation of Pd(553): From Ultrahigh Vacuum to Atmospheric Pressure. *Phys. Rev. B* **2007,** *76* (15), 155410.
38. Westerstrom, R.; Weststrate, C. J.; Gustafson, J.; Mikkelsen, A.; Schnadt, J.; Andersen, J. N.; Lundgren, E.; Seriani, N.; Mittendorfer, F.; Kresse, G.; Stierle, A., Lack of Surface Oxide Layers and Facile Bulk Oxide Formation on Pd(110). *Phys. Rev. B* **2009,** *80* (12), 125431.
39. Eastman, J. A.; Fuoss, P. H.; Rehn, L. E.; Baldo, P. M.; Zhou, G. W.; Fong, D. D.; Thompson, L. J., Early-Stage Suppression of Cu (001) Oxidation. *Appl. Phys. Lett.* **2005,** *87*, 051914.